Aalborg Universitet

Correlating structure with mechanical properties in lithium borophosphate glasses

Liu, Pengfei; Youngman, Randall E.; Jensen, Lars Rosgaard; Smedskjær, Morten Mattrup

Link to publication from Aalborg University

SPECIAL ISSUE ARTICLE

Correlating structure with mechanical properties in lithium borophosphate glasses

Pengfei Liu[1] ⬡ | **Randall E. Youngman**[2] ⬡ | **Lars R. Jensen**[3] ⬡ |
Morten M. Smedskjaer[1] ⬡

[1]Department of Chemistry and
Bioscience, Aalborg University, Aalborg,
Denmark

[2]Science and Technology Division,
Corning Incorporated, Corning, New
York, USA

[3]Department of Materials and Production,
Aalborg University, Aalborg, Denmark

Correspondence
Morten M. Smedskjaer, Department of
Chemistry and Bioscience, Aalborg
University, Aalborg, Denmark.
Email: mos@bio.aau.dk

Funding information
China Scholarship Council, Grant/Award
Number: 201806370210

Abstract

Connecting structure with mechanical properties is needed for improving the
mechanical reliability of oxide glasses. Although the mechanical properties of
silicate and borosilicate glasses have been intensively studied, this is not the
case for phosphate and borophosphate glasses. To this end, we here study the
structure, density, glass transition, hardness, elasticity, and cracking behavior
of lithium borophosphate glasses. The glasses are designed with different B/P
ratios to access different boron and phosphorus speciation. The introduction of
boron in the phosphate network increases the average network rigidity because
of the reduction in the fraction of nonbridging oxygens as well as the exchange of
phosphate groups with more constrained BO_4 groups. These structural changes
result in an increase in density, Vickers hardness, glass transition temperature,
and Young's modulus, and a decrease in Poisson's ratio for higher B_2O_3 content.
Furthermore, the increase in network rigidity and atomic packing density results
in a lower ability of the glasses to densify upon indentation, resulting in an overall
decrease in crack initiation resistance. Finally, we find an increase in the fraction
of trigonal boron units in the high-B_2O_3 glasses, which has a significant effect on
atomic packing density and Vickers hardness.

KEYWORDS

borophosphate glasses, indentation, mechanical properties, structure, structure–property
relations

1 | INTRODUCTION

Oxides glasses are hard and chemically durable mate-
rials that have been used in many applications, from
automotive and architectural window glasses to protec-
tive screens for electronic devices and optical fibers in
high-speed internet cables. The relatively low practical
strength and limited toughness of glasses can be ascribed
to the existence of surface flaws and the lack of a stable
shearing deformation mechanism.[1] Glass scientists have
therefore been interested in discovering and designing
stronger and tougher glass materials. The compositional
design of new glasses is a promising method to improve
its mechanical properties because the glass composition

can be designed using a wide variety of elements from the periodic table.[2] However, the relationship among glass composition, atomic structure, and mechanical properties remains poorly understood, despite the advances in especially structural characterization of the disordered atomic structure of glasses.

Despite not being as industrially important as silicate glasses, borate glasses have been applied in certain applications, such as batteries, metal seals, and biomedical components,[3–5] due to their relatively low melting temperature and similar thermal expansion coefficient with many metals or ceramics. In addition, borate glasses exhibit some interesting structural features, including (i) rich medium and short-range structures[6–8] and (ii) highly temperature-,[9] humidity-,[10,11] and pressure[12–14]-sensitive network structure. These characteristics have given rise to the discovery of some borate glass series with good inherent damage resistance, such as boroaluminosilicate[15–17] and alkali aluminoborate compositions.[18–20] Among them, aluminoborate glasses[11,19] have been shown to feature a highly structurally adaptive response to an applied stress, particularly as a result of a pressure-induced increase in the boron coordination numbers, which helps to improve the crack initiation resistance. That is, glasses with higher content of trigonal boron units tend to have higher crack initiation resistance than those with more tetrahedral boron units. Moreover, cesium aluminoborate glasses possess ultrahigh crack resistance after humid aging posttreatment.[10,11] In some compositional ranges, the borate network structure cannot accommodate more tetrahedral boron units and, thus, forms nonbridging oxygens (NBOs), which depolymerize the glassy network structure. Previous studies[21,22] have found that the NBO content also affects the mechanical properties of the glass, with low NBO content promoting densification during the indentation process and thereby improving the crack initiation resistance. Furthermore, there are various superstructural units in borate glasses, which also affect the glass properties, including bulk density, glass transition temperature, thermal expansion coefficient, and ionic conductivity.[23–25]

Our previous work[26] found that the coordination numbers of Al and B increase significantly under an applied pressure or stress in lithium phosphoaluminoborate glasses with high content of P_2O_5. Indeed, the volume densification experienced by these glasses can to a large extent be ascribed to these coordination number changes, whereas a smaller fraction of the volume densification can be ascribed to such changes in silicate glasses.[12] Understanding the structure densification mechanism of oxide glasses plays a key role in controlling their deformation mechanism and cracking behavior.[27–29] Therefore, in this work, we studied lithium borophosphate glasses. Our study focuses on the effect of the boron-to-phosphorus ratio (for a constant lithium oxide content) on the glass structure and mechanical properties. Specifically, we have measured density (ρ), atomic packing density (C_g), glass transition temperature (T_g), elastic properties, Vickers hardness (H_v), and crack initiation resistance (CR) as well as Raman and $^6Li/^7Li$, ^{11}B and ^{31}P magic angle spinning (MAS) nuclear magnetic resonance (NMR) spectroscopy of lithium borophosphate glasses.

We note that previous works[30,31] have studied the formation, glass transition temperature, structure, and electrical conductivity of lithium borophosphate glasses, showing that the introduction of boron leads to more P–O–B and B–O–B bonding but less P–O–P bonding and fewer NBOs. This results in increasing T_g and electrical conductivity. However, the correlation between structure and mechanical properties of this glass series is still missing. To design stronger and tougher glasses, the key challenge is to establish a structural understanding of glass fracture mechanics at all relevant length scales, including the relation between structural transformations and various mechanical properties. The present study, therefore, provides new insights, for example, regarding the role of P–O–B bonding on glass hardness and crack initiation resistance.

2 | EXPERIMENTAL PROCEDURES

2.1 | Glass preparation

In this study, a variety of lithium borophosphate glasses were synthesized by using the traditional melt-quenching technique. That is, $45Li_2O–(55−x)P_2O_5–xB_2O_3$ with $x = \{0, 5.5, 11, 16.5, 22\}$ (in mol%). The utilized raw materials were Li_2CO_3 (≥98.5%, Merck KGaA), H_3BO_3 (≥99.5%, Honeywell International), and NH_6PO_4 (≥99.5%, Merck KGaA). First, the previous raw materials were weighed according to the calculation and fully mixed. Then, the mixed ingredients were gradually added to the preheated alumina crucible, which was used to avoid damage of Pt crucibles for these compositions at high temperature. The crucible was placed in a furnace at 800°C for around 1 h to remove H_2O, CO_2, and NH_3. Next, the mixed batch was melted at 950–1100°C for 0.5–1 h in air, and then this melt with low viscosity was poured onto a steel plate for the quenching process. The prepared glasses were quickly transferred to a preheated annealing furnace and heated at the estimated T_g for around 30 min and then slowly cooled down to room temperature.

Subsequently, we used differential scanning calorimetry measurements (STA 449 F3 Jupiter, Netzsch) to determine the glass transition temperature (T_g) of all obtained glasses in Pt crucibles (in argon with a gas flow rate of 60 ml min^{-1}) at a constant heating/cooling rate of 10 K min^{-1}. The

TABLE 1 Analyzed chemical compositions of the lithium borophosphate glasses (in mol%)

45Li$_2$O–xB$_2$O$_3$–(55 − x)P$_2$O$_5$ in mol%				
Glass ID	B$_2$O$_3$	P$_2$O$_5$	Li$_2$O	Al$_2$O$_3$
LiPB-0	0.0	52.8	46.4	0.7
LiPB-5.5	5.2	47.9	46.3	0.5
LiPB-11	10.9	42.4	46.5	0.1
LiPB-16.5	16.4	37.4	45.8	0.4
LiPB-22	21.7	32.2	44.0	2.1

Note: The uncertainty is around ±.2%.

recorded isobaric heat capacity (C_p) curves are shown in Figure S1. We have summarized the T_g values and other property data in Table S1. After determining T_g, all obtained glasses were reannealed at the measured T_g values for 30 min and then cooled down to room temperature at a rate of around 3 K min^{-1}.

Finally, all reannealed glasses were cut to the needed dimensions and polished to an optical finish in 99.9% ethanol by using SiC grinding paper (grits 220, 500, 800, 1200, 2400, and 4000). Furthermore, the chemical compositions of all as-made glasses were analyzed using inductively coupled plasma optical emission spectroscopy for B$_2$O$_3$ and P$_2$O$_5$ and flame emission spectroscopy for the determination of Li$_2$O content (see Table 1). In addition, we also used the inductively coupled plasma mass spectrometry method to further determine the content of Al$_2$O$_3$ in all samples (from crucible contamination) and any trace content of B$_2$O$_3$ in the LiPB-0 glass. These contents have also been included in Table 1. Due to the volatility of B and P at high temperatures, we can find some minor differences between the nominal and analyzed compositions. In addition, we measured a small amount of Al$_2$O$_3$ in all the glasses, especially in the LiPB-22 glass, indicating that the molten glass had reacted with the alumina crucible at high temperatures. We also melted glasses with higher borate content, but in these cases, the alumina content became unacceptably high and we therefore focus on the five glasses in Table 1 in this work.

2.2 | Density and atomic packing density

Archimedes buoyancy principle was used to determine the density (ρ) of the glass samples. To this end, we first measured the weight of each sample (at least 3 g) at least 10 times in both 99.9% ethanol and atmosphere (atmospheric pressure, 23°C). Subsequently, we calculated the molar volume (V_m) from the ratio of molar mass to density. Next, to better analyze the difference of free volume between these glasses, we calculated the atomic packing density (C_g). This calculation was made by assuming twofold coor-

dination for O and sixfold coordination for Li, whereas we used the NMR results (see later) to extract the coordination numbers for B, P, and Al. C_g is then defined as the ratio between the theoretical molar volume occupied by ions (assumed to be spherical) and the effective molar volume of the glass,

$$C_g = \rho \frac{\sum f_i V_i}{\sum f_i M_i} \quad (1)$$

where $V_i = \frac{4}{3} \pi N(x r_A^3 + y r_B^3)$ represents the molar volume of an oxide $A_x B_y$ with the molar fraction f_i and the molar mass M_i, N denotes Avogadro's number, and r_A and r_B are the ionic radii of the cations and anions, respectively, which are taken from Shannon.[32]

2.3 | X-ray diffraction

We obtained X-ray diffraction (XRD, Empyrean XRD, PANalytical) patterns of all glass specimens from 2.5 to 80° at 40 kV with a scanning speed of 8° min^{-1}. We could not identify any signs of crystallization from the XRD results (Figure S2). Furthermore, all obtained glasses were transparent and showed no signs of liquid–liquid phase separation.

2.4 | Raman spectroscopy

Raman spectra were collected using a micro-Raman spectrometer (inVia, Renishaw). The sample surface was excited by a 532-nm green He–Ne laser for an acquisition time of 10 s. The range of the spectrum was from 250 to 1750 cm^{-1}, and the resolution was better than 2 cm^{-1}. Spectra from five different surface locations were accumulated for each glass to ensure homogeneity. All spectra were uniformly treated in Origin software for background correction and area normalization. No significant differences across the sample surface were observed, suggesting that the glasses are compositionally homogeneous (see Figure S3).

2.5 | Solid-state NMR spectroscopy

^{11}B MAS NMR experiments were conducted at 16.4 T by using a commercial spectrometer (DD2, Agilent) and a commercial triple-resonance 3.2-mm MAS NMR probe (Agilent). The resonance frequency for ^{11}B at this external magnetic field was 224.52 MHz. Glasses were powdered with an agate mortar and pestle and then loaded into zirconia rotors for sample spinning at 20 kHz. Data were

collected with short radio-frequency pulse widths of .6 μs ($\pi/12$ tip angle) and relaxation delays of 4 s for ^{11}B. Signal averaging was performed using 600–1000 scans per experiment.

^{6}Li and ^{7}Li MAS NMR spectra were also collected at 16.4 T using the same configuration as for ^{11}B NMR above. Powdered glasses in 3.2-mm zirconia rotors were spun at 22 and 15 kHz for ^{7}Li and ^{6}Li NMR, respectively. ^{7}Li MAS NMR, with a resonance frequency of 272.0 MHz, was performed using $\pi/6$ pulse widths (1 μs), delays of 10 s, and 32 acquisitions. ^{6}Li MAS NMR spectra, at a resonance frequency of 103.0 MHz, were acquired using pulse lengths of 1.5 μs ($\pi/6$ tip angle), recycle delays of 600 s to accommodate the much longer spin-lattice relaxation times, and 100 acquisitions.

^{31}P MAS NMR data were acquired using a commercial console (VNMRS, Varian) and a 3.2-mm MAS NMR probe (Chemagnetics), in conjunction with an 11.7 T wide bore superconducting magnet and a resonance frequency of 202.30 MHz. Powdered glasses were contained in 3.2-mm zirconia rotors and sample spinning was controlled to 20 kHz. Measurement conditions included $\pi/6$ pulse widths of 1.2 μs, recycle delays of 60 s, and acquisition of nominally 1500 scans.

MAS NMR spectra for the different nuclei were processed without any additional apodization, plotted using the normal shielding convention, and with shift referencing to aqueous boric acid (19.6 ppm), aqueous lithium chloride (.0 ppm), and 85% H_3PO_4 solution (.0 ppm). ^{11}B MAS NMR data were fit with DMFit[33] utilizing second-order quadrupolar lineshapes for ^{11}B trigonal peaks and a combination of Gaussian and Lorentzian lineshapes for ^{11}B tetrahedral resonances. The overlapping satellite transition spinning sideband for the B^{IV} resonance[34] was also fit and subtracted from the integration, yielding accurate site intensities for all B^{III} and B^{IV} peaks. ^{31}P MAS NMR data were fit using DMFit and 100% Gaussian lineshapes. Due to the substantial overlap of ^{31}P resonances, fitting was performed using peak positions for the two end-member glasses and literature values for different lithium phosphate groups, as discussed later. The width and shift of each ^{31}P resonance were held in a narrow range to facilitate fitting and estimates for the different phosphate groups.

2.6 | Elastic modulus

The glasses' elastic properties were measured by ultrasonic echography using an ultrasonic thickness gauge (38DL Plus, Olympus) equipped with 20-MHz delay line transducers for the determination of the longitudinal V_1 and transversal V_2 wave velocities. The longitudinal modulus C_{11}, shear modulus G, bulk modulus B, and Young's modulus E, as well as the Poisson ratio ν, were calculated using the following relations, which are applicable for isotropic materials:

$$C_{11} = \rho V_1^2, \tag{2}$$

$$G = \rho V_2^2, \tag{3}$$

$$B = C_{11} - \frac{4}{3}G, \tag{4}$$

$$\nu = \frac{3B - 2G}{6B + 2G}, \tag{5}$$

$$E = 2G(1 + \nu). \tag{6}$$

2.7 | Vickers hardness

The Vickers hardness of the glasses was measured by using the Nanovea CB500 hardness tester. First, we produced 15 indents on each specimen with a maximum load of 0.98 N (0.1 kgf), where the loading duration and dwell time were 6 and 10 s, respectively. Subsequently, the residual imprints were analyzed immediately after unloading (20–30 s) with an optical microscope, allowing us to calculate H_ν as

$$H_\nu = 1.8544 \frac{P}{\left(\frac{d_1 + d_2}{2}\right)^2}, \tag{7}$$

where P is the load of 0.98 N, and d_1 and d_2 are the length of the projected indent diagonals.

2.8 | Crack initiation resistance

Next, we produced 10 indents at different loads on each specimen with a Vickers diamond tip (loading duration of 6 s and dwell time of 10 s) to evaluate the crack initiation resistance (CR). The measurements were conducted under laboratory conditions (room temperature, relative humidity of 35 ± 5%RH). We calculated the probability of crack initiation (PCI) at each load by using the method of Wada et al.,[35] where PCI is the ratio between the number of corners with a corner crack and the total number of corners (4 for Vickers). Then, CR is defined as the load when there are two cracks on average for each Vickers indent (PCI = 50%).

3 | RESULTS AND DISCUSSION

3.1 | Raman spectroscopy

First, we used micro-Raman spectroscopy to study the structural differences in the lithium borophosphate glasses with different B/P ratios. Figure 1A shows the micro-Raman spectra of the investigated glasses. To better analyze the Raman results, we divide the micro-Raman spectra into three main band regions, and the results are shown in the following. It should be noted that phosphate glasses are usually composed of PO_4 tetrahedra. These are denoted as Q^n groups, with n representing the number of bridge oxygen atoms shared by two neighboring P.

The low-frequency band region I mainly contains the structural units associated with bending of PO_4 units,[26] cation oxygen polyhedra and $(P_2O_7)^{4-}$ groups,[36,37] and (P–O–P)$_{sym}$ in Q^2 units.[37] In this frequency range, we only observe one band and the relative intensity of this band decreases with the content of B_2O_3, consistent with a smaller concentration of PO_4 units.

Next, we observe that the intermediate-frequency band region II (~400–820 cm^{-1}) contains two different bands, where the Raman shift and intensity of these two bands depend on the B/P ratio. In the LiPB-0 glass without B_2O_3, the band region IIa (~690 cm^{-1}) is characteristic for symmetric stretching vibrations of P–O–P bonds,[36–39] such as (P–O–P)$_{sym}$ stretch (bridging oxygen) with Q^1 species and (P–O–P)$_{sym}$ stretch (bridging oxygen) with Q^2 species. We found that the intensity of this band decreases as the concentration of B_2O_3 increases. In the LiPB-11 glass, the addition of B_2O_3 begins to have a significant effect on the glass structure as evident from the change in the shape of band region II. In addition, we found in the

LiPB-16.5 glass that the peak IIa is replaced with two new peaks at ~660 (IIb) and ~750 (IIc) cm^{-1}. The peak IIb is associated with a phosphate chain connected to the BO_4 unit, whereas the peak IIc is typically assigned to borate superstructures.[7,40–42] Furthermore, we find that the formation of boron superstructures and phosphate chains connected to the BO_4 units result in a wider band region II upon B_2O_3 addition.

Finally, in the high-frequency band region III (~820–1400 cm^{-1}),[36] we clearly find that there are two distinct bands (IIIa and IIIb) in low-B_2O_3 glass (LiPB-0 to LiPB-16.5 glasses), whereas one new band (IIIc) can be observed in high-B_2O_3 glass (LiPB-16.5 glass) because of peak broadening and position changes (see Figure 1B). The Raman shifts and intensity of these two bands depend on the B/P ratio. In the LiPB-0 glass, the band region IIIa (~1175 cm^{-1}) is expected to result from vibrations of the symmetric stretching mode of P–O–P NBOs, such as (PO$_3$)$_{sym}$ stretch (NBO) with Q^1 species, (PO$_2$)$_{sym}$ stretch (NBO) with Q^2 species, P–O stretch with Q^1 chain terminator, and "strained" (PO$_2$)$_{sym}$.[43] The band region IIIc (~1030 cm^{-1}) is expected to be due to the borate superstructures.[44,45] With an increase in the B_2O_3 content, we find that the position of the band region IIIa shifts toward lower frequencies (Figure 1B), indicating the formation of BO_4 units. In addition, upon increasing the B_2O_3 content, the formation of BPO_4 and $(P_2O_7)^{4-}$ units around 1100 (in LiPB-16.5 glass) and 1030 cm^{-1} (in LiPB-22 glass) is observed, resulting in a wider band region III upon B_2O_3 addition. Finally, the high-frequency band region IIIb (~1265 cm^{-1}) can likely be ascribed to vibrations of the symmetric stretch of the P–O terminal oxygens ((P = O)$_{sym}$ stretch) and (PO$_2$)$_{asym}$ stretch (NBO) with Q^2 species. The relative intensity of this band region becomes smaller at higher B_2O_3 content.
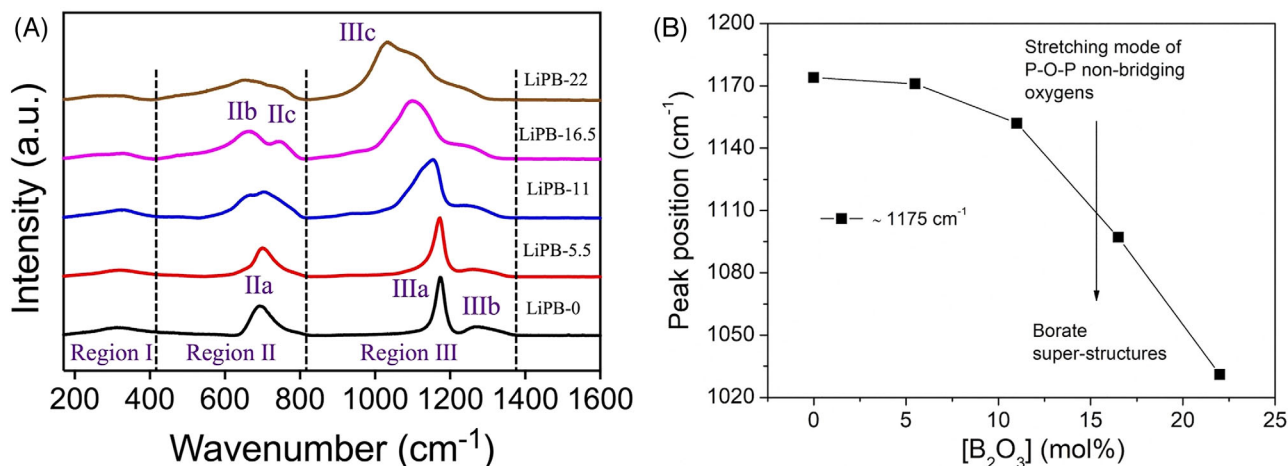

FIGURE 1 (A) Micro-Raman spectra and (B) peak position of the micro-Raman band around 1175 cm^{-1} for the annealed lithium borophosphate glasses as a function of the B_2O_3 content
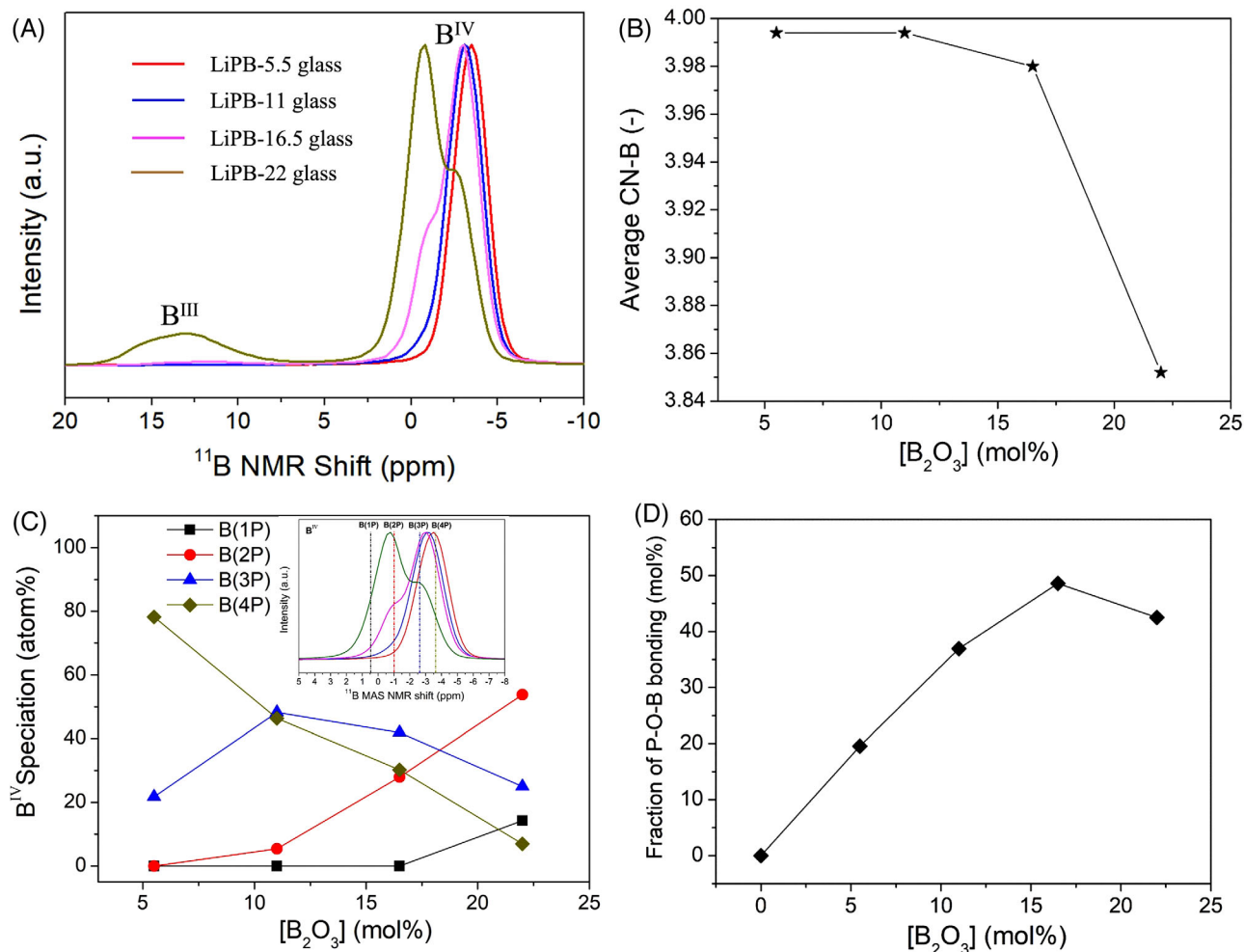
FIGURE 2 (A) ^{11}B magic angle spinning (MAS) nuclear magnetic resonance (NMR) spectra for the boron-containing lithium borophosphate glasses. (B) Composition dependence of the average coordination numbers of boron. (C) Composition dependence of the population of four B^{IV} species. Inset: ^{11}B MAS NMR spectra with four distinct B^{IV} species indicated by the dotted vertical lines. (D) Composition dependence of the fraction of P–O–B bonds as calculated from Equation (8)

3.2 | ^{11}B MAS NMR spectroscopy

To better analyze the short-range structure difference in the investigated series of glasses with varying B/P ratios, we have performed ^{11}B, ^{31}P, and ^{6}Li (^{7}Li) MAS NMR measurements. The determined speciation for B and P are given in Tables S2–S4.

Figure 2A shows the ^{11}B MAS NMR spectra related to the four boron-containing glasses. In the three low-B_2O_3 glasses (LiPB-5.5 to LiPB-16.5 glasses), the boron speciation mainly consists of B^{IV} units (around −3.5 to −3 ppm, >98%). In the LiPB-22 glass, we observe the appearance of a significant fraction of B^{III} units (around 13 ppm) due to the continuous increase in the content of B_2O_3. In other words, the average coordination number of boron decreases with the addition of B_2O_3 (Figure 2B), indicating that the increase in the content of B_2O_3 will lead to the

conversion of B^{IV} to B^{III}, especially in the LiPB-22 glass. This is likely because the boron network formers compete with phosphorus for the Li$^+$ modifiers, and for high-B_2O_3 glasses, the amount of Li–B^{IV} interaction is insufficient, thus the modification level of borate polyhedra is low. Furthermore, a small amount of Al_2O_3 contamination (less than ∼2 mol%) from the crucible could be another contributing factor to the conversion of B^{IV} to B^{III}, especially in the LiPB-22 glass (Table 1). That is, similar to traditional Al-bearing glasses, each Al atom requires Li$^+$ for charge-balancing, thus resulting in fewer available Li$^+$ to convert B^{III} to B^{IV}. On the other hand, it is well known in aluminophosphate glasses that charge-balancing of both Al and P polyhedra can be achieved without the need for modifiers (e.g., Li$^+$). In this scenario, the small amount of Al_2O_3 contamination could increase the concentration of available Li$^+$, leading to an increase in B^{IV}, or possibly B^{III} with

NBO. In order to better understand the structural impact of Al_2O_3 contamination in these glasses, we have measured the ^{27}Al MAS NMR spectrum of the LiBP-22 glass (Figure S4), which shows three resonances corresponding to Al in four-, five-, and six-fold coordination. The positions of these peaks, especially when considering the magnetic field used for the NMR experiment, indicate substantial interaction between Al polyhedra and phosphate groups. That is, the AlO_4 peak around 42 ppm and the AlO_6 resonance at −13 ppm are both shifted significantly to higher shielding as a result of next–nearest neighbor phosphate groups, as is typical in aluminophosphate glasses. Thus, the likely presence of Al–O–P bonding could slightly increase the amount of Li^+ available to interact with B— one reason to avoid such complications in the glasses with higher levels of Al_2O_3 contamination. However, given the relatively low concentration of Al_2O_3 in these glasses (Table 1), the impact on B and P coordination is minimal. As the B_2O_3 content increases, we observe other changes (peak B^{IV} position and shape) in the ^{11}B MAS NMR spectra (see Figure 2A). The fitting of the ^{11}B MAS NMR spectra (see Table S3 and Figure S5) helps us to understand these structural changes, because B^{IV} can be deconvoluted into four distinct species in this series of glasses. Figure 2C shows the composition dependence of the four distinct B^{IV} species, as well as the corresponding ^{11}B MAS NMR spectra.

We clearly observe that the position of the B^{IV} units shifts to lower shielding (from −3.5 to −0.8 ppm) with increasing B_2O_3 content (from 0 to 22 mol%), indicating a close relation to the interaction between phosphate groups and B^{IV} units.[46] In fact, our previous work[47] has shown that the P NNNs (phosphorus species present as next nearest neighbors) group have a strong shielding effect on B^{IV} units. That is, the interactions of phosphate groups with B^{IV} units result in a more negative shift. Therefore, as B_2O_3 content increases in this series of glasses, B(4P) will be converted into B(3P), B(2P), and eventually B(1P) (where B(nP) means one B atom surrounded by n P atoms as NNNs, see Table S3), which can result in the shape of the B^{IV} units to change and reduce the shielding effect on B^{IV} units. In addition, the glass composition also influences the B^{III} signal. In Figure 2A, this may not be obvious, but it can be clearly observed from the fitting of the ^{11}B MAS NMR data (Table S2 and Figure S5) that the B^{III} peak can be deconvoluted into two different B^{III} units. Therefore, the addition of B_2O_3 leads to a direct increase in the content of B^{III} resonance, which includes symmetric B^{III} (all bridging oxygen) and asymmetric B^{III} (two bridging oxygens and one NBO). Furthermore, increasing the content of B_2O_3 at the expense of P_2O_5 leads to a higher relative content of the asymmetric B^{III} groups, though the relative peak areas for the two B^{III} resonances (Table S2) have large uncertainties.
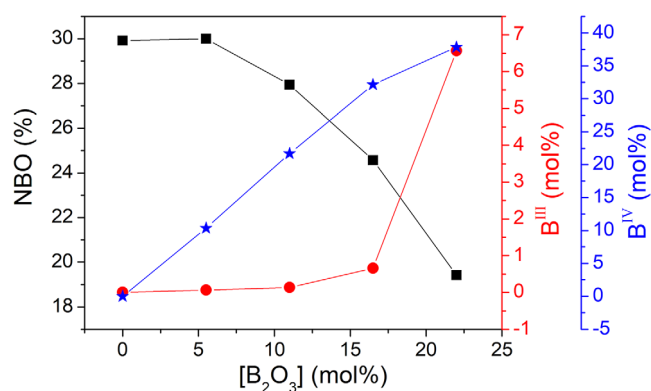

FIGURE 3 Composition dependence of the fractions of the number of total nonbridging oxygens (NBOs) and molar concentration of B^{III} and B^{IV} units. The latter are calculated from the glass compositions (Table 1) and boron speciation data derived from ^{11}B magic angle spinning (MAS) nuclear magnetic resonance (NMR) measurements (Table S2).

To better understand the connectivity between B and P polyhedra in this series of glasses, we have calculated the molar fractions of the P–O–B bonds based on the following equation and the data from the NMR analyses. The result is shown in Figure 2D. This fraction first increases and then decreases with the amount of B_2O_3 in this series of glasses. In the LiPB-22 glass, the molar fraction of P–O–B bonds slightly decreases, likely due to the decrease in the amount of P_2O_5 and the coordination environment change of the boron (the conversion of B^{IV} to B^{III}), as well as the formation of the new linkages of type B-(OP)$_3$ together with B–O–B bonds.[31] This is because the B/P association does not typically involve B^{III} units.[48] This shows that the connectivity between B and P polyhedra strongly depends on the composition.

$$P - O - B \ (mol\%) = 2 \times B_2O_3 \ (mol\%) \times BO_4 \ (atom\%)$$

$$\times \left[\frac{1}{2} B(1P) + B(2P) + \frac{3}{2} B(3P) + 2B(4P) \right] (atom\%)$$

(8)

Finally, we have studied the influence of the addition of B_2O_3 on the fraction of total NBOs in the glasses (Figure 3). According to the results from Tables 1 and S2, we have calculated the fraction of total NBOs and molar concentration of B^{III} and B^{IV} units. In the borate-based glasses, the network structure cannot accommodate more tetrahedral boron units and at that point, NBOs are instead formed. Therefore, in these glasses, all Li^+ ions are used to charge-compensate BO_4 groups or form NBOs (i.e., on P). Some B^{IV} units will likely interact with P to form BPO$_4$-like units, where the B and P effectively charge-balance each other and, thus, consume fewer modifiers (Li^+ ions). Therefore,
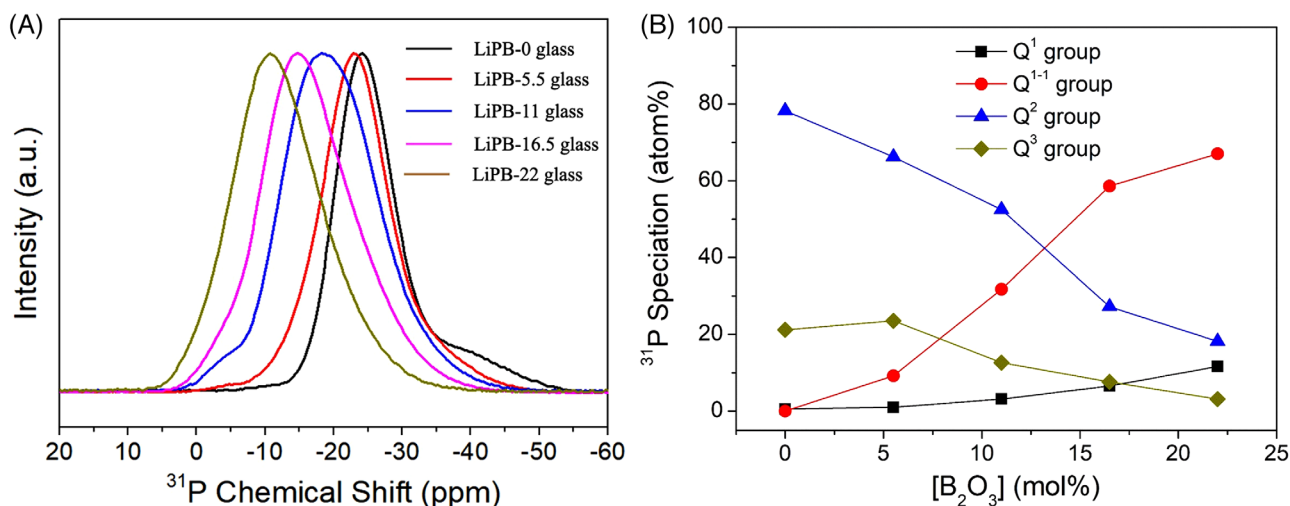
FIGURE 4 (A) ^{31}P magic angle spinning (MAS) nuclear magnetic resonance (NMR) spectra of the lithium borophosphate glasses. (B) Composition dependence of the relative fractions of the phosphorus Q^n species as determined by deconvoluting the ^{31}P MAS NMR spectra.

in this study, the fraction of total NBOs is estimated as follows:

$$NBOs_{total} = \frac{X_{Li^+} - (X_{BO_4} - X_{BPO_4})}{X_{O^{2-}}}, \quad (9)$$

where X_i is the molar fraction of species i in the glass. In Equation (9), the numerator calculates the total fraction of Li^+ minus the part of BO_4 units used for charge-balancing Li^+ (i.e., as BPO_4 units are not requiring charge-balancing from Li^+). Based on Figure 2C, this assumes that only B(4P) units belong to BPO_4-like units, and thus all other BO_4 units take Li^+ from the phosphate groups. It is important to note that we do not include the NBO contribution from asymmetric B^{III} units, which are believed to be present in the high-B_2O_3 glasses but are difficult to accurately quantify.

B_2O_3 addition leads to an increase in both molar concentrations of B^{IV} and B^{III} (especially in the LiPB-22 glass, see Figure 3). Therefore, we find in this study that the fraction of total NBOs decreases overall with the addition of B_2O_3 due to the increase in the molar concentration of tetrahedral boron units. This is consistent with the micro-Raman result that the band region IIIa shifts toward lower frequencies. Furthermore, in the LiPB-5.5 glass, the fraction of total NBOs increases slightly (from 29.9% to 30.0%) upon the addition of B_2O_3. To understand the composition dependence of NBOs, we note that the initial B_2O_3 addition is mainly in the form of B(4P) units with a smaller fraction of other BO_4 units. This explains why the total number NBOs does not initially change much, that is, because the added boron barely needs any charge-balancing from Li^+. As more B_2O_3 is added, more of the non-B(4P) groups form, thus interacting with more

of the Li^+ modifiers and reducing the total number of NBOs.

3.3 | ^{31}P MAS NMR spectroscopy

Figure 4A presents the ^{31}P MAS NMR spectra of the lithium borophosphate glasses, with an example of the deconvolution for the LiBP-16.5 glass shown in Figure S6. First, we find that the average main peak position of the ^{31}P MAS NMR spectra shifts to a less negative value (from -24 to -11 ppm) upon the addition of B_2O_3. Due to the competition for Li^+ modifiers between boron and phosphorus species (as well as aluminum in LiPB-22 glass), the geometry of phosphate tetrahedra and the connected (neighboring) polyhedra, that is, Q^n speciation of the phosphate groups, may be affected by the glass composition. As seen earlier in the analysis of boron speciation, boron speciation is greatly impacted by Li^+ enabling the formation of B^{IV} tetrahedra. In the normal P-free borate and borosilicate glasses, all BO_4 groups require charge-balancing, and thus other network polyhedra will be further polymerized. In this study, the B_2O_3 was added to LiPB-0 glass and boron speciation shows an increase in the mole fraction of BO_4 groups, indicating that the added B_2O_3 did indeed remove a fraction of the Li^+ modifier from the phosphate portion of the network when a higher content of B_2O_3 (>5.5 mol%) is introduced. However, these Q^3 and Q^2 units of the phosphate groups were converted to lower Q^n units, indicating that phosphate groups are depolymerized upon the addition of B_2O_3.

The composition dependence of the fraction of different phosphorus Q^n species[49,50] is shown in Figure 4B, which supports the previous point. This is because more P units

interact with B units upon the addition of B_2O_3, which leads to a significant increase in the relative fraction of the Q^{1-1} groups (Q^1 phosphate group with one B NNN) as shown in Figure 4B. In the LiPB-0 glass, the main peak position is found at about −24 ppm, which is between those of Q^2 (∼22 ppm) and Q^3 (∼30 ppm) polyhedra.[49,51] Therefore, if the influence of neighboring polyhedra is neglected, this result shows that there is a mixture of Q^2 and Q^3 phosphate groups in the LiPB-0 glass. Another important factor affecting the ^{31}P chemical shift is the effect of the combination of boron cations with phosphate groups. Four main possibilities for connecting boron groups to phosphorus exist, which in turn determine their chemical shift. First, we observe that the main peak of ^{31}P widened with the addition of B_2O_3, which is attributed to the increase in the number of boron species as NNNs of phosphorus groups. Here, according to the deconvolution of the ^{31}P peak, we assign a peak at around −5 ppm to Q^1 groups[49] without any B NNNs, another peak at around −22 ppm to Q^2 groups[49] without any B NNNs, and a peak at around −30 ppm to Q^3 groups[51] without any B NNNs. This suggests that there is a larger number of P−O−P bonds in this glass series. In addition, we assign the more intense peak at around −15 ppm to Q^{1-1} groups, that is, a Q^1 phosphate group with one B NNN. As shown in Figure 4B, the relative fractions of Q^2 and Q^3 phosphate units decrease, whereas that of Q^1 and Q^{1-1} groups increase upon the addition of B_2O_3. This indicates that the addition of B_2O_3, that is, the removal of P_2O_5, results in the conversion of Q^2 and Q^3 phosphate units to Q^1 and Q^{1-1} groups (the formation of pyrophosphate), and consequently, the average peak position of ^{31}P shifts positively (from −24 to −11 ppm) with increasing B_2O_3 content from 0 to 22 mol%. These results are in good agreement with the variation in P−O−B bonds and NBOs fraction as determined from the ^{11}B MAS NMR data.

3.4 | [6]Li and ^{7}Li MAS NMR spectroscopy

Due to the homonuclear dipolar coupling of higher abundance [7]Li nucleus,[52] the [6]Li MAS NMR spectrum tends to yield narrower resonances and better spectral resolution.[49,53] Figure 5 presents [6]Li MAS NMR spectra for the lithium borophosphate glasses, showing a systematic, downfield shift in the [6]Li resonance with composition. ^{7}Li MAS NMR data (see Figure S7) show the same systematic shift with composition. In both sets of spectra, these peaks all exhibit a single broad isotropic resonance centered at −0.7 to −0.9 ppm, which are assigned to LiO_4 or LiO_5 polyhedra.[54] In the LiPB-0 glass, there is a noticeable asymmetry in the [6]Li MAS NMR peak (or multiple peaks) related to different Li^+ sites around the various
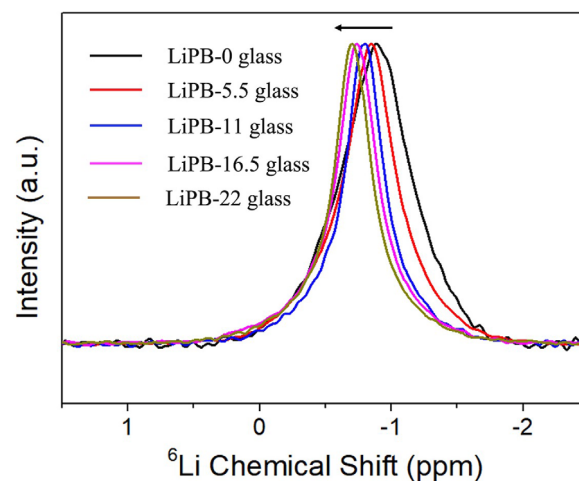

FIGURE 5 [6]Li magic angle spinning (MAS) nuclear magnetic resonance (NMR) spectra for the lithium borophosphate glasses. The arrow indicates the change in the direction of increasing B_2O_3 content.

phosphate groups.[54] Furthermore, we find that the main peak of [6]Li MAS NMR spectra becomes sharper and shifts toward lower shielding (from −0.9 to −0.7 ppm) with the addition of B_2O_3, indicating that the addition of B_2O_3 results in decreasing average coordination number of Li and/or decreasing Li−O distance (positive shift of this peak), in turn reflecting an increase in the covalency of the Li−O bonding.[49] Furthermore, the B_2O_3 results in some changes in the distribution of the Li^+ environment (i.e., more narrow resonance or collapse of multiple peaks into a single peak). This is because the distribution of phosphate Q^n groups becomes narrower (i.e., phosphate groups are depolymerized from Q^3/Q^2 to Q^{1-1}/Q^1 units) upon the addition of B_2O_3, which decreases the types of anionic network polyhedra. This may lead to a more uniform coordination environment of lithium atoms. In addition, the network polymerization of phosphate groups will increase the chemical shift of the [6]Li MAS NMR spectrum.[54]

3.5 | Atomic packing

Figure 6 shows the density (ρ), molar volume (V_m), and atomic packing density (C_g) of the lithium borophosphate glasses with different B/P ratios. As seen in the figure, density increases monotonically as a function of the concentration of B_2O_3 except for the LiPB-22 glass. This trend is attributed to the result of the competition between B_2O_3 and P_2O_5. That is, B-for-P substitution decreases the glass' molar mass (P_2O_5 is heavier than B_2O_3) but increases the degree of packing in the LiPB-0 to LiPB-16.5 glasses, which leads to an increase in the bulk density. However, especially for the LiPB-22 glass, we measure some amount
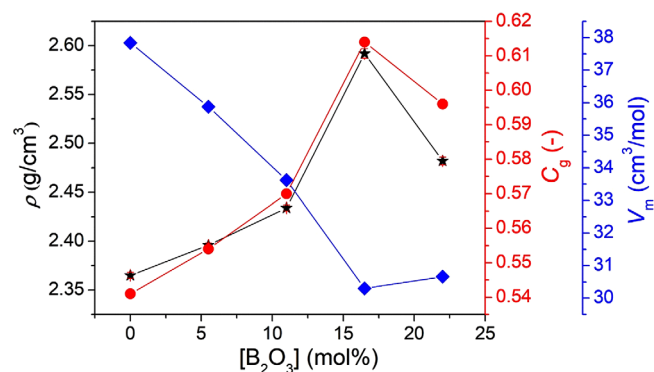
FIGURE 6 Composition dependence of density (ρ), molar volume (V_m), and atomic packing density (C_g) for lithium borophosphate glasses

of Al_2O_3 (Table 1), which could lead to the decrease in the density, because the addition of Al_2O_3 will decrease the molar mass of the glass (LiPB-16.5 glass is heavier than Al_2O_3) and decrease the degree of packing in the low-Al_2O_3 glass.[18]

Furthermore, we can find some changes in the molar mass with the B_2O_3 concentration. Therefore, we calculate the molar volume (V_m) to evaluate these changes in the overall glassy network packing. The molar volume features a decrease with increasing B_2O_3 content, showing that the glassy network structure becomes more compact upon the B_2O_3 addition. Finally, due to differences in the size and coordination environment of the atoms with composition, we have also calculated the atomic packing density (C_g) to clarify the difference in the network packing efficiency. We find from Figure 6 that C_g has the same trend with the density, that is, C_g first increases and then decreases with the B_2O_3 level.

3.6 | Glass transition temperature and elastic properties

Figure 7A shows the compositional evolution of the glass transition temperature (T_g) in lithium borophosphate glasses, revealing a remarkable increase in the B_2O_3 content. This is well-aligned with the formation of a more rigid glassy network upon the addition of B_2O_3. That is, there will be more atomic constraints per atom and volume as a result of the higher extent of cross-linking through the formation of P–O–B bonds. In previous studies, it has been shown that a more rigid glassy network is positively correlated with higher T_g.[25] Furthermore, BO_4 units are topologically more constrained than any of the phosphate Q^n groups,[55–57] suggesting the higher glass transition temperature upon the addition of B_2O_3. As such, we find an apparent positive correlation in Figure 7B between T_g

and the fraction of more constrained network polyhedra (BO_4 units).

Next, we consider the variation in Young's modulus (E) and Poisson's ratio (ν) by using the ultrasonic echography method. Figure 7A also shows the composition dependence of Young's modulus (E) and Poisson's ratio (ν). Bond strength, the number of bonds per volume, and network rigidity influence the elastic moduli.[58–60] The density and atomic packing density of this series of glasses show an overall upward trend with the B_2O_3 level, which leads to the larger number of bonds per volume and thus contributes to the increase in Young's modulus. Furthermore, Young's modulus is also positively correlated with the content of more constrained network polyhedra (BO_4 units), which strongly supports the previous point (Figure 7B). Finally, the increase in the B_2O_3 concentration also influences Poisson's ratio, although the value of all glasses is within a relatively narrow range (0.240–0.265). Poisson's ratio shows a negative correlation with the content of B_2O_3, that is, the opposite composition trend compared to E and T_g. The rigid and highly cross-linked networks with high T_g and E values will also result in low Poisson's ratio.[60] In addition, Figure 7B shows that Poisson's ratio decreases monotonically with the content of more constrained network polyhedra (BO_4 units). This negative correlation can be ascribed to the changes in network rigidity because the addition of B_2O_3 leads to an overall reduction in NBOs and the formation of P–O–B bonds and BO_4 units, which in turn result in the rigid network. Moreover, Poisson's ratio in this series of glasses shows a negative correlation with atomic packing density (see Figure S8), which is abnormal behavior.[60] That is, the previous work[61] suggests that there is an overall positive correlation between atomic packing density and Poisson's ratio. For example, the increase of atomic packing density can result from decreasing lengths of modifier oxygen bonds,[62] which in turn can lead to increasing Poisson's ratio. In this series of glasses, the atomic packing density increases with the addition of B_2O_3, which should increase Poisson's ratio. However, replacing any type of phosphate group with a BO_4 tetrahedron will also increase the network rigidity, which usually decreases Poisson's ratio.[60] It, therefore, appears that the latter effect dominates, thus resulting in a negative correlation between atomic packing density and Poisson's ratio (abnormal behavior).

3.7 | Vickers hardness

Figure 8A shows the Vickers hardness of the studied glass series. The B_2O_3 addition has a positive effect on the Vickers hardness, and Vickers hardness also has the same trend as the atomic packing density (Figure 8B). That is, a
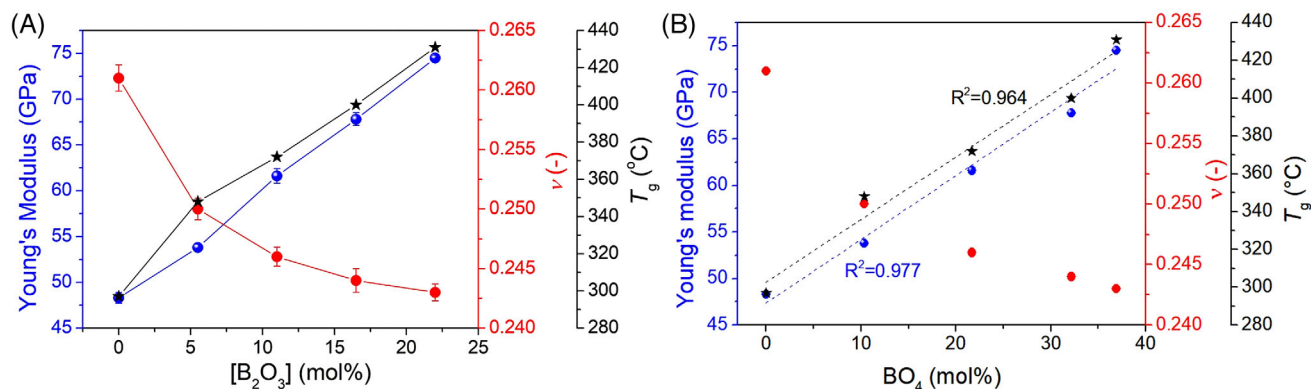
FIGURE 7 (A) Composition dependence of Young's modulus (E), Poisson's ratio (ν), and glass transition temperature (T_g) of the lithium borophosphate glasses. The error in T_g does not exceed 2°C. (B) Dependence of Young's modulus (E), Poisson's ratio (ν), and glass transition temperature (T_g) on the fraction of BO$_4$ units
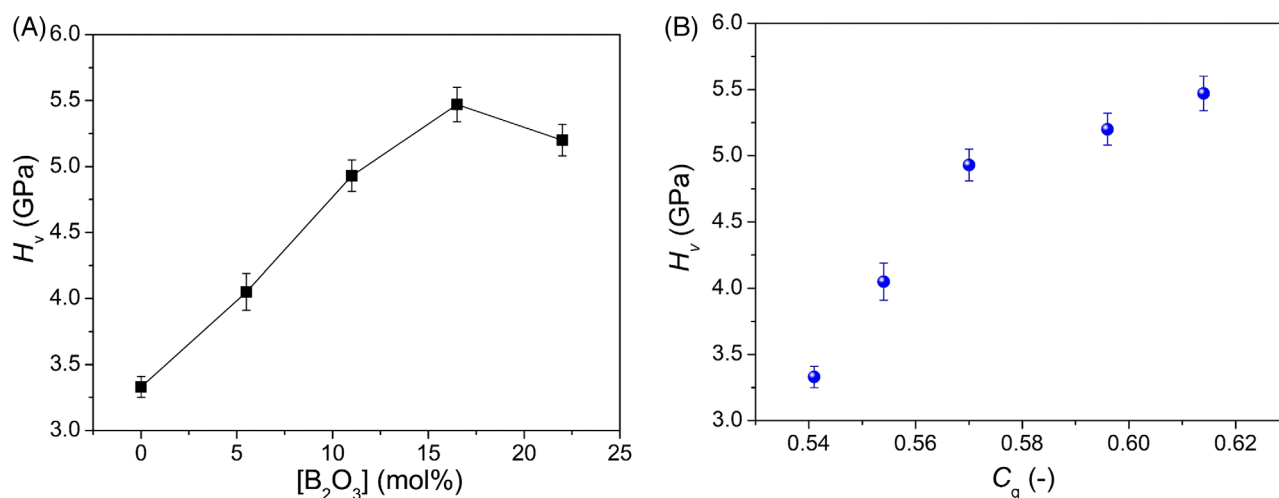

FIGURE 8 (A) Composition dependence of Vickers hardness (H_v) for lithium borophosphate glasses. (B) Dependence of Vickers hardness (H_v) on atomic packing density (C_g)

high atomic packing density results in a higher number of atomic bonds per volume. Furthermore, hardness is a measure of the ability of glass to resist permanent deformation, and the content of NBOs decreases, and the content of rigid BO$_4$ units increases upon B$_2$O$_3$ addition, which increases the rigidity of the glassy network. In general, these results support the view that bond density and network rigidity are the key factors affecting the hardness of glasses.[63]

3.8 | Indentation cracking

Due to the mismatch between the amount of plastic deformation and the surrounding elastic deformation,[64,65] crack initiation in the glass will occur under critical loads. As expected based on the previous work[27] and the values of E/H and ν in this study, the dominant crack-types are the radial and lateral ones in the studied glasses. Figure S9 shows images of the generated corner cracks, which supports this point. Furthermore, as the content of B$_2$O$_3$ increases, the lateral cracking could seem to become more apparent, which might be due to the decrease in Poisson's ratio.[27] Figure 9 shows the crack initiation resistance (*CR*) (calculated from Figure S10) for the present lithium borophosphate glasses. We observe that the B$_2$O$_3$ addition has a pronounced effect on *CR*, that is, *CR* shows an overall negative trend with the B$_2$O$_3$ level. Previous works[19,21,66,67] have shown that network flexibility, network self-adaptability, and densification ability under pressure or stress have an important influence on the crack initiation ability of oxide glasses. That is, glasses with good network flexibility, network self-adaptability, and densification ability will better dissipate damage energy during the sharp contact process, thereby improving the
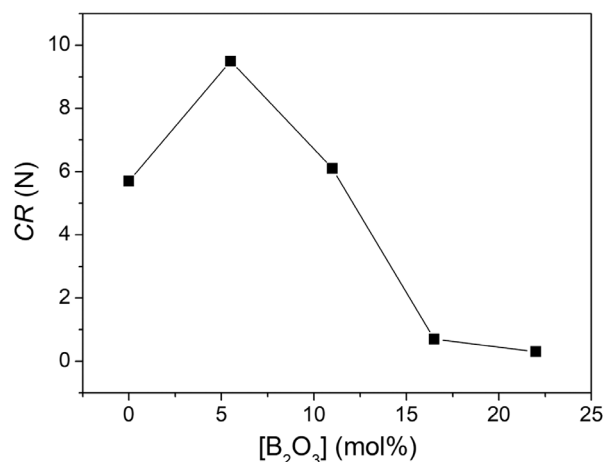
FIGURE 9   Composition dependence of the crack resistance (CR) for lithium borophosphate glasses. The estimated error in CR is 20% of its value.

crack initiation resistance. In this study, the network rigidity of this glass series increases with the B_2O_3 level due to the reduction in the fraction of NBOs and the formation of new P–O–B bonds as well as more rigid BO_4 units (relative to the exchanged phosphate groups), which is expected to decrease the network flexibility of this series of glass and may decrease the crack resistance. In addition, the atomic packing density of this series of glasses shows an increasing trend with the addition of B_2O_3, leading to a denser and more rigid network structure, which will reduce their densification ability under stress. The glass that is prone to densification under pressure can generally reduce the residual stress around the indent, thereby improving the crack resistance.[19,68] In more details, the densification ability strongly depends on the content of trigonal boron units, as B^{III} units are prone to transition to B^{IV} units under pressure/stress.[62,69] This is beneficial for crack resistance. However, as shown in Figure S11, the fraction of B^{III} species is negatively correlated with crack resistance, indicating that the interaction of phosphate groups with B^{IV} units and the content of NBOs strongly affect the crack initiation ability of the as-made glasses. Finally, besides the general decrease in CR with the amount of B_2O_3, there is a local maximum in CR. The structural origin of this apparent maximum is unknown.

4 | CONCLUSIONS

In this study, we have studied the network structure and mechanical properties of $45Li_2O–xB_2O_3–(55 − x)P_2O_5$ glasses with varying B/P ratios. To this end, we have performed Raman and NMR ($^{6,7}Li$, ^{11}B, ^{31}P) spectroscopic analyses as well as density, ultrasonic echography, and Vickers indentation measurements. We find from the

Raman spectroscopy data that the B_2O_3 addition disturbed the phosphate network, with the NMR data showing a reduction of NBOs and the formation of new P–O–B bonds. Overall this feature, as well as the replacement of BO_4 units for phosphate groups, increases the average network rigidity and also the density, Vickers hardness, glass transition temperature, and Young's modulus, whereas a decrease in Poisson's ratio is observed. In addition, we find that the phosphate groups are partially depolymerized from Q^3/Q^2 units to Q^{1-1}/Q^1 units upon B_2O_3 addition. The total reduction of NBOs, from decreasing concentration of phosphate Q^n groups and increasing BO_4 units, is expected to reduce the network flexibility of this series of glass, and the increase of the C_g will decrease the densification ability of the glasses under pressure/stress, which in turn results in an overall decrease in crack resistance. Finally, we find an increase in the fraction of B^{III} units (the conversion of B^{IV} to B^{III}) in the LiPB-22 glass, reducing the number of P–O–B bonds, which in turn leads to a decrease in atomic packing density and Vickers hardness. However, we also note that especially this glass composition contains a small amount (2 mol%) of alumina contamination from the crucible, complicating the analyses. In any case, our work shows overall that the network rigidity, NBOs, and boron coordination environment play important roles in controlling the mechanical properties of the lithium borophosphate glasses.

ORCID
Pengfei Liu https://orcid.org/0000-0003-2885-4721
Randall E. Youngman https://orcid.org/0000-0002-6647-9865
Lars R. Jensen https://orcid.org/0000-0003-1617-0306
Morten M. Smedskjaer https://orcid.org/0000-0003-0476-2021

REFERENCES
1. Kurkjian CR, Gupta PK, Brow RK, Lower N. The intrinsic strength and fatigue of oxide glasses. J Non-Cryst Solids. 2003;316(1):114–24.
2. Zanotto ED, Coutinho FAB. How many non-crystalline solids can be made from all the elements of the periodic table?. J Non-Cryst Solids. 2004;347(1–3):285–8.
3. Brow RK, Tallant DR. Structural design of sealing glasses. J Non-Cryst Solids. 1997;222:396–406.
4. Jones JR, Clare AG. Bioactive borate glasses. Bio-glasses: an introduction. New York: Wiley, 2012. p. 75–95.

5. Kim JG, Son B, Mukherjee S, Schuppert N, Bates A, Kwon O, et al. A review of lithium and non-lithium based solid state batteries. J Power Sources. 2015;282:299–322.

6. Konijnendijk WL, Stevels JM. The structure of borate glasses studied by Raman scattering. J Non-Cryst Solids. 1975;18(3):307–31.

7. Meera BN, Ramakrishna J. Raman spectral studies of borate glasses. J Non-Cryst Solids. 1993;159(1–2):1–21.

8. Wright AC. My borate life: an enigmatic journey. Int J Appl Glass Sci. 2015;6(1):45–63.

9. Sen S, Xu Z, Stebbins JF. Temperature dependent structural changes in borate, borosilicate and boroaluminate liquids: high-resolution ^{11}B, ^{29}Si and ^{27}Al NMR studies. J Non-Cryst Solids. 1998;226(1–2):29–40.

10. Januchta K, Stepniewska M, Jensen LR, Zhang Y, Somers MA, Bauchy M, et al. Breaking the limit of micro-ductility in oxide glasses. Adv Sci. 2019;6(18):1901281.

11. Liu P, Youngman RE, Jensen LR, Bockowski M, Smedskjaer MM. Achieving ultrahigh crack resistance in glass through humid aging. Phys Rev Mater. 2020;4(6):063606.

12. Wu J, Gross TM, Huang L, Jaccani SP, Youngman RE, Rzoska SJ, et al. Composition and pressure effects on the structure, elastic properties and hardness of aluminoborosilicate glass. J Non-Cryst Solids. 2020;530:119797.

13. Lee SK, Eng PJ, Mao H, et al. Probing of bonding changes in B_2O_3 glasses at high pressure with inelastic X-ray scattering. Nat Mater. 2005;4(11):851–4.

14. Kapoor S, Guo X, Youngman RE, Hogue SL, Rzoska SJ, Obckowski M, et al. Network glasses under pressure: permanent densification in modifier-free Al_2O_3-B_2O_3-P_2O_5-SiO_2 systems. Phys Rev Appl. 2017;7(5):054011.

15. Zheng Q, Potuzak M, Mauro JC, Smedskjaer MM, Youngman RE, Yue Y. Composition-structure-property relationships in boroaluminosilicate glasses. J Non-Cryst Solids. 2012;358(6–7):993–1002.

16. Liu P, Januchta K, Jensen LR, Bauchy M, Smedskjaer MM. Competitive effects of free volume, rigidity, and self-adaptivity on indentation response of silicoaluminoborate glasses. J Am Ceram Soc. 2020;103(2):944–54.

17. Smedskjaer MM. Topological model for boroaluminosilicate glass hardness. Front Mater. 2014;1:1–6.

18. Januchta K, Youngman RE, Goel A, et al. Structural origin of high crack resistance in sodium aluminoborate glasses. J Non-Cryst Solids. 2017;460:54–65.

19. Januchta K, Youngman RE, Goel A, et al. Discovery of ultra-crack-resistant oxide glasses with adaptive networks. Chem Mater. 2017;29(14):5865–76.

20. Mohan S, Kaur S, Singh DP, Kaur P. Structural and luminescence properties of samarium doped lead alumino borate glasses. Opt Mater (Amst). 2017;73:223–33.

21. Kato Y, Yamazaki H, Yoshida S, Matsuoka J. Effect of densification on crack initiation under Vickers indentation test. J Non-Cryst Solids. 2010;356(35–36):1768–73.

22. Sellappan P, Rouxel T, Celarie F, Becker E, Houizot P, Conradt R. Composition dependence of indentation deformation and indentation cracking in glass. Acta Mater. 2013;61(16):5949–65.

23. Boulos EN, Kreidl NJ. Structure and properties of silver borate glasses. J Am Ceram Soc. 1971;54(8):368–75.

24. Shelby JE. Thermal expansion of alkali borate glasses. J Am Ceram Soc. 1983;66(3):225–7.

25. Mauro JC, Gupta PK, Loucks RJ. Composition dependence of glass transition temperature and fragility. II. A topological model of alkali borate liquids. J Chem Phys. 2009;130(23):234503.

26. Liu P, Søndergaard ALS, Youngman RE, et al. Structural densification of lithium phosphoaluminoborate glasses. J Am Ceram Soc. 2021;104(3):1345–59.

27. Rouxel T. Driving force for indentation cracking in glass: composition, pressure and temperature dependence. Philos Trans R Soc, A. 2015;373(2038):20140140.

28. Bauchy M, Micoulaut M. Transport anomalies and adaptive pressure-dependent topological constraints in tetrahedral liquids: evidence for a reversibility window analogue. Phys Rev Lett. 2013;110(9):095501.

29. Svenson MN, Thirion LM, Youngman RE, et al. Pressure-induced changes in interdiffusivity and compressive stress in chemically strengthened glass. ACS Appl Mater Interfaces. 2014;6(13):10436–44.

30. Tho TD, Prasada Rao R, Adams S. Structure property correlation in lithium borophosphate glasses. Eur Phys J E. 2012;35(1):8.

31. Muñoz F, Montagne L, Pascual L, Durán A. Composition and structure dependence of the properties of lithium borophosphate glasses showing boron anomaly. J Non-Cryst Solids. 2009;355(52–54):2571–7.

32. Shannon RD. Revised effective ionic radii and systematic studies of interatomic distances in halides and chalcogenides. Acta Crystallogr, Sect A. 1976;32(5):751–67.

33. Massiot D, Fayon F, Capron M, King I, Le Calvé S, Alonso B, et al. Modelling one- and two-dimensional solid-state NMR spectra. Magn Reson Chem. 2002;40(1):70–6.

34. Massiot D, Bessada C, Coutures JP, Taulelle F. A quantitative study of ^{27}Al MAS NMR in crystalline YAG. J Magn Reson (1969). 1990;90(2):231–42.

35. Wada M, Furukawa H, Fujita K. Crack resistance of glass on Vickers indentation. In: Proceedings of the 10th international congress on glass. vol. 11, no. 39. Tokyo: Ceramic Society of Japan; 1974.

36. Ardelean I, Rusu D, Andronache C, Ciobotă V. Raman study of xMeO·(100-x)$[P_2O_5·Li_2O]$ (MeO⇒Fe_2O_3 or V_2O_5) glass systems. Mater Lett. 2007;61(14–15):3301–4.

37. Lai YM, Liang XF, Yang SY, Wang JX, Zhang BT. Raman spectra study of iron phosphate glasses with sodium sulfate. J Mol Struct. 2012;1013:134–7.

38. Brow RK, Tallant DR, Myers ST, Phifer CC. The short-range structure of zinc polyphosphate glass. J Non-Cryst Solids. 1995;191(1–2):45–55.

39. Silva AMB, Correia RN, Oliveira JMM, Fernandes MHV. Structural characterization of TiO_2-P_2O_5-CaO glasses by spectroscopy. J Eur Ceram Soc. 2010;30(6):1253–8.

40. Konijnendijk WL, Stevels JM. The structure of borosilicate glasses studied by Raman scattering. J Non-Cryst Solids. 1976;20(2):193–224.

41. Vignarooban K, Boolchand P, Micoulaut M, Malki M, Bresser WJ. Rigidity transitions in glasses driven by changes in network dimensionality and structural groupings. EPL (Europhys Lett). 2014;108(5):56001.

42. Krogh-Moe J. The structure of vitreous and liquid boron oxide. J Non-Cryst Solids. 1969;1(4):269–84.

43. Cozar O, Magdas DA, Nasdala L, Ardelean I, Damian G. Raman spectroscopic study of some lead phosphate glasses with tungsten ions. J Non-Cryst Solids. 2006;352(28–29):3121–5.

44. Li H, Su Y, Li L, Strachan DM. Raman spectroscopic study of gadolinium (III) in sodium-aluminoborosilicate glasses. J Non-Cryst Solids. 2001;292(1–3):167–76.

45. Kamitsos EI, Chryssikos GD. Borate glass structure by Raman and infrared spectroscopies. J Mol Struct. 1991;247(C):1–16.

46. Michaelis VK, Kachhadia P, Kroeker S. Clustering in borate-rich alkali borophosphate glasses: a ^{11}B and ^{31}P MAS NMR study. Phys Chem Glasses. 2013;54(1):20–6.

47. Liu P, Søndergaard ALS, Youngman RE, Rzoska SJ, Bockowski M, Jensen LR, et al. Structural densification of lithium phospho-aluminoborate glasses. J Am Ceram Soc. 2021;104(3):1345–59.

48. Uesbeck T, Eckert H, Youngman R, Aitken B. The structure of borophosphosilicate pure network former glasses studied by multinuclear NMR spectroscopy. J Phys Chem C. 2017;121(3):1838–50.

49. van Wüllen L, Eckert H, Schwering G. Structure-property correlations in lithium phosphate glasses: new insights from ^{31}P ↔ ^{7}Li double-resonance NMR. Chem Mater. 2000;12(7):1840–6.

50. Zeyer-Düsterer M, Montagne L, Palavit G, Jäger C. Combined ^{17}O NMR and ^{11}B-^{31}P double resonance NMR studies of sodium borophosphate glasses. Solid State Nucl Magn Reson. 2005;27(1–2):50–64.

51. Brow RK. Review: the structure of simple phosphate glasses. J Non-Cryst Solids. 2000;263–4:1–28.

52. Michaelis VK, Levin K, Germanov Y, Lelong G, Kroeker S. Ultrahigh-resolution ^{7}Li magic-angle spinning nuclear magnetic resonance spectroscopy by isotopic dilution. Chem Mater. 2018;30(16):5521–6.

53. Xu Z, Stebbins JF. ^{6}Li nuclear magnetic resonance chemical shifts, coordination number and relaxation in crystalline and glassy silicates. Solid State Nucl Magn Reson. 1995;5(1):103–12.

54. Alam TM, Conzone S, Brow RK, Boyle TJ. ^{6}Li, ^{7}Li nuclear magnetic resonance investigation of lithium coordination in binary phosphate glasses. J Non-Cryst Solids. 1999;258(1–3):140–54.

55. Jiang Q, Zeng H, Liu Z, Ren J, Chen G, Wang Z, et al. Glass transition temperature and topological constraints of sodium borophosphate glass-forming liquids. J Chem Phys. 2013;139(12):124502.

56. Hermansen C, Youngman RE, Wang J, Yue Y. Structural and topological aspects of borophosphate glasses and their relation to physical properties. J Chem Phys. 2015;142(18):184503.

57. Smedskjaer MM, Mauro JC, Youngman RE, Hogue CL, Potuzak M, Yue Y. Topological principles of borosilicate glass chemistry. J Phys Chem B. 2011;115(44):12930–46.

58. Wilkinson CJ, Zheng Q, Huang L, Mauro JC. Topological constraint model for the elasticity of glass-forming systems. J Non-Cryst Solids: X. 2019;2:100019.

59. Yang K, Yang B, Xu X, Hoover C, Smedskjaer MM, Bauchy M. Prediction of the Young's modulus of silicate glasses by topological constraint theory. J Non-Cryst Solids. 2019;514:15–9.

60. Rouxel T. Elastic properties and short-to medium-range order in glasses. J Am Ceram Soc. 2007;90(10):3019–39.

61. Østergaard MB, Hansen SR, Januchta K, To T, Rzoska SJ, Bockowski M, et al. Revisiting the dependence of Poisson's ratio on liquid fragility and atomic packing density in oxide glasses. Materials. 2019;12(15):2439.

62. Svenson MN, Bechgaard TK, Fuglsang SD, Pedersen RH, Tjell ØA, Østergaard MB, et al. Composition-structure-property relations of compressed borosilicate glasses. Phys Rev Appl. 2014;2(2):024006.

63. Kapoor S, Wondraczek L, Smedskjaer MM. Pressure-induced densification of oxide glasses at the glass transition. Front Mater. 2017;4:1–20.

64. Limbach R, Winterstein-Beckmann A, Dellith J, Möncke D, Wondraczek L. Plasticity, crack initiation and defect resistance in alkali-borosilicate glasses: from normal to anomalous behavior. J Non-Cryst Solids. 2015;417–418:15–27.

65. Cook RF, Pharr GM. Direct observation and analysis of indentation cracking in glasses and ceramics. J Am Ceram Soc. 1990;73(4):787–817.

66. Bechgaard TK, Goel A, Youngman RE, Mauro JC, Rzoska SJ, Bockowski M, et al. Structure and mechanical properties of compressed sodium aluminosilicate glasses: role of non-bridging oxygens. J Non-Cryst Solids. 2016;441:49–57.

67. Yoshida S, Sanglebœuf J-C, Rouxel T. Quantitative evaluation of indentation-induced densification in glass. J Mater Res. 2005;20(12):3404–12.

68. Aakermann KG, Januchta K, Pedersen JAL, Svenson Mouritz N, Rzoska SJ, Bockowski M, et al. Indentation deformation mechanism of isostatically compressed mixed alkali aluminosilicate glasses. J Non-Cryst Solids. 2015;426:175–83.

69. Kato Y, Yamazaki H, Kubo Y, Yoshida S, Matsuoka J, Akai T. Effect of B_2O_3 content on crack initiation under Vickers indentation test. J Ceram Soc Jpn. 2010;118(9):792–8.

SUPPORTING INFORMATION

Additional supporting information can be found online in the Supporting Information section at the end of this article.